COMPARISON OF CHARGE COLLECTION IN A SI AVALANCHE PHOTODIODE FOR ALPHA-PARTICLE AND PHOTON IRRADIATION

By

Richard H. Nederlander

Thesis

Submitted to the Faculty of the
Graduate School of Vanderbilt University
in partial fulfillment of the requirements
for the degree of

MASTER OF SCIENCE
in
ELECTRICAL ENGINEERING

December 18, 2021

Nashville, TN

Approved:

Robert A. Reed, Ph.D.
Ronald D. Schrimpf, Ph.D.

ACKNOWLEDGEMENTS

Many individuals deserve recognition for their support in the successful completion of this research. First, none of this work would have been possible without the dedicated tutelage, guidance, and mentorship of my advisors: Professor Robert Reed and Professor Keivan Stassun. Even before Day 1 of graduate school, when I was an REU intern during the summer of 2017, they showed an avid interest in my growth into a professional researcher. I am very appreciative that they enabled me to find a project that intertwined my interests in electrical engineering and astrophysics.

I would also like to extend gratitude to many members of the Radiation Effects and Reliability (RER) group at Vanderbilt University, as well as graduate students, professors, and postdoctoral researchers at Fisk University. Dr. Dennis Ball II, Professor Brian Sierawski, and Professor Ronald Schrimpf provided keen insight and critiques into my work that challenged my thinking and allowed it to progress. Professor Enxia Zhang provided essential help in preparing the photodiode for radiation testing. Frank Padgett III was tremendously helpful in assisting with collecting experimental data. Professor Arnold Burger, Professor Rastgo Hawrami, and Dr. Liviu Matei provided me with a thorough understanding of the latest engineering and astrophysics research in this field.

I am also appreciative of the guidance received from senior graduate students. Specifically, Kaitlyn Ryder and Andrew Tonigan taught me the tools and techniques necessary to properly build the simulations and conduct the experiments necessary for this work. Overall, I am very thankful for the time that these professors, postdoctoral researchers, and graduate students took to help me.

These acknowledgements would not be complete without mentioning my family. I would like to thank my Dad, my Mom, my brother William, and my sister Ava.

And finally, I am grateful for the financial support received from the Air Force Research Lab, the Air Force Office of Scientific Research, and the Vanderbilt Initiative in Data-Intensive Astrophysics (VIDA). I am also grateful to both Vanderbilt University and Fisk University for opening their facilities to me in support of this work.

TABLE OF CONTENTS

LIST OF FIGURES

CHAPTER I

INTRODUCTION

Silicon avalanche photodiodes (Si APDs) are semiconductor p-n junction devices that convert photons into amplified electrical current by enhancing generated charge via avalanche. They are intrinsically immune to magnetic fields and achieve an internal avalanche gain greater than 50 at low noise levels, which is a function of the APD's doping profile (Figure I.1). This profile is created using spreading resistance measurements. These features give APDs a size, weight, and power advantage over non-avalanche photodiodes. This is partially because APDs do not need amplifiers to observe pulses.

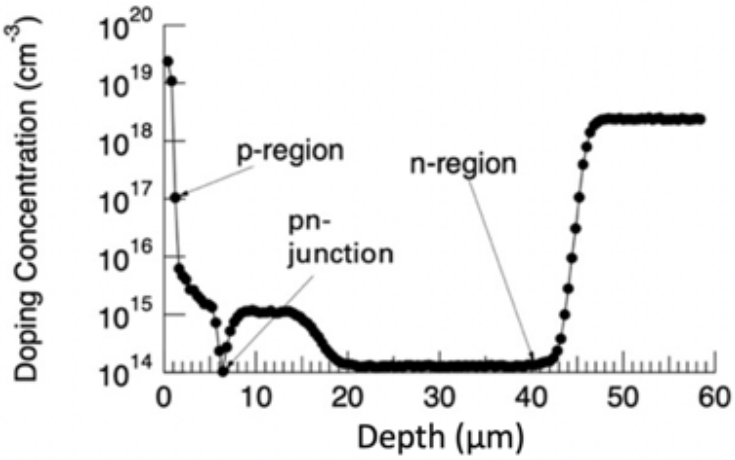

Figure I.1. Doping profile of the characterized Si APD created using spreading resistance.

These advantages make Si APDs a vital component in satellites for lidar (Light Detecting and Ranging) applications and optical communications [1], as well as for astrophysics experiments [2]. For this study, we consider a CubeSat mission developed at Vanderbilt University [2] to detect thermal neutrons using a $^{6}LiInSe_2$ scintillator crystal. The purpose is to allow Vanderbilt astrophysicists to measure the free neutron lifetime to an accuracy of 1% by determining the photon production from neutron interactions with a scintillator crystal using a Si APD [2]. Since low-Earth orbit (LEO) has a low thermal neutron density ($2.2*10^{-4}$ /s/cm^2) [3], an avalanche photodiode is selected for this mission.

It is important to note that the space radiation environment may mask the APD's desired photon signal. This concern can be better understood after comparing photon transient response to ion irradiation. The APD's non-avalanche counterpart have already been used in a variety of space missions. One use-case includes the imaging sensors in the Hubble Space Telescope [4]. These imaging sensors incorporate HgCdTe photodiode arrays that help enable Hubble to observe in the short-wave infrared (SWIR) to mid-wave infrared (MWIR) wavelength region [4]. Another application is a precision-calibrated silicon photodiode used in the PanSTARRS telescope's Gigapixel imager. It is used as a metrology reference to allow the telescope to determine the relative throughput of stars within the 400 nm to 1050 nm wavelength range [5]. And currently, an initiative is underway between NASA's Goddard Space Flight Center (GSFC) and Leonardo DRS Electro-Optical Infrared Systems to develop HgCdTe APD arrays for space lidar receivers [6].

To this end, an APD (a Hamamatsu Photonics device with type number S8664-1010) is irradiated with ~5.5 MeV alpha particles from a 10 μCi Am^{241}. The APD's charge collection as a function of bias is found to differ from that from photons. This study looks at this difference by comparing the Si APD's charge collection mechanisms. Charge enhancement for the alpha particles is found to be reduced because the field where most of the charge is generated is not capable of providing significant generated charge via avalanche. Meanwhile, the field can generate a larger number of carriers sufficient for avalanche for a continuous photon source. Temporal characteristics (e.g., rise time) is used to compare the two sources' responses.

CHAPTER II

BACKGROUND

II.1 Understanding the Si APD's Physical Mechanisms

To understand the charge collection mechanisms taking place within the Si APD, we must first understand the physics behind the APD's abilities. They include photon absorption, Shockley-Read-Hall recombination, and avalanche breakdown. Each plays a role in converting photons to electrons, passing electrons through the device, and amplifying the electron signal, respectively. Chapter II will review each concept separately, define charge collection explicitly, and review the literature on prior experiments that observed this phenomenon in an Si APD.

II.2 History of the APD

Before we continue, we need to understand the historical creation of the APD. The research that led to the avalanche photodiode began in 1887 with the discovery of the photoelectric effect by Hertz [7]. Realizing that certain materials can convert light to electrical signals, engineers began looking into designs that could utilize this phenomenon. One of these early designs was the photomultiplier tube (PMT). It is important to note that the physical processes behind APDs and PMTs greatly differ despite their shared ability to absorb photons and release electrons in response (which will be referred to as photon absorption). Specifically, the former is based on photodiode technology (invented in the early 1940s [8]) and the latter is based on vacuum tube technology (invented in 1904 [9]). Because vacuum tube technology was invented earlier, research was conducted earlier into enabling this effect to occur in vacuum tube technology (e.g., the PMT). Once this effect was applied to photodiode technology, engineers found it to have distinct advantages over the PMT (which will be discussed below).

The PMT was invented in 1936 by Zworykin [10], and it was incorporated into a variety of instruments: radar jammers (during World War II), scintillation counters (for nuclear physics), and headlight dimmers (for adjusting a car's headlights/taillights based on the ambient light around the car, but rarely used today) [11]. Today, PMTs are used in medical equipment (e.g., Positron

Emission Tomography and in-vitro assay), high-energy physics experiments (e.g., colorimeters), and industrial measurement systems (e.g., laser scanners) [12].

Depending on its design, the PMT can achieve gains of 10^7 and higher at low noise [13]. Due to this high avalanche gain output, the PMT is best equipped for low light-level conditions in UV to IR wavelengths [13]. However, the PMT is prone to issues that make it unideal for various high energy/high radiation environments. These issues include its delicate and complex design (resulting in costs potentially greater than ~$1,500) [14], and a susceptibility to magnetism [12]. As a result, the APD is preferred due to its immunity to magnetism and relatively lower costs [15].

The APD was patented in 1952 by Nishizawa [16]. Its creation was made possible by the theories proposed by Shockley, Read, Hall, McKay, and McAfee (among many others). These theories include generation-recombination in the space-charge region [17], and the multiplication effects in pn junctions [18]. They helped lead to the photodiode by providing theoretical insight into their innerworkings. Modifications to the photodiode design enabled the avalanche effect, thereby leading to the avalanche photodiode.

II.3 Photon Absorption Definition

Photon absorption occurs in a device's photosensitive region in response to photons interacting with it. The photons eject electrons with an energy proportional to the illuminating photons' frequency (Figure II. 1) [19]. This electrical current only occurs when photons meet or exceed a threshold frequency specific to the semiconductor's material, which in our case is silicon [19]. For the Si APD used in this study, the cutoff wavelength is 600 nanometers [20]. Furthermore, one electron-hole pair is created per 3.6 eV of energy transferred through a silicon photodiode at 300 Kelvin. This effect is seen in the device's bandgap diagram (Figure II. 2), which will be presented in the next section.

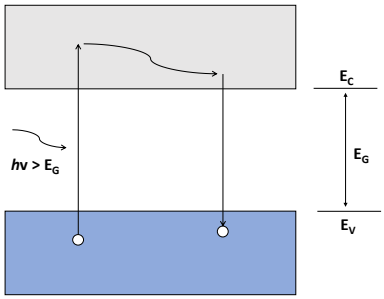

Figure II. 1: Schematic of photon absorption.

II.4 Shockley-Read-Hall Recombination

The bandgap diagram of this study's Si APD can provide an understanding of the processes by which electrons (in this case, the ones generated from photon absorption) move through the device. Figure II. 2 presents the bandgap diagram simulated by TCAD of the APD, based on its doping profile. This diagram is composed of a conduction band, a valence band, and a Fermi level E_F. The conduction band is the uppermost band while the valence band is the lowermost band. The length of time taken for an electron to travel between these bandgap edges is determined by recombination and generation processes. For the APD studied here, one of the most important processes to consider is the Shockley-Read-Hall (SRH). SRH recombination is important because it is directly influenced by the number of energy states in the semiconductor. This is more of a consideration for SRH than the other recombination and generation processes, for reasons that will be discussed below.

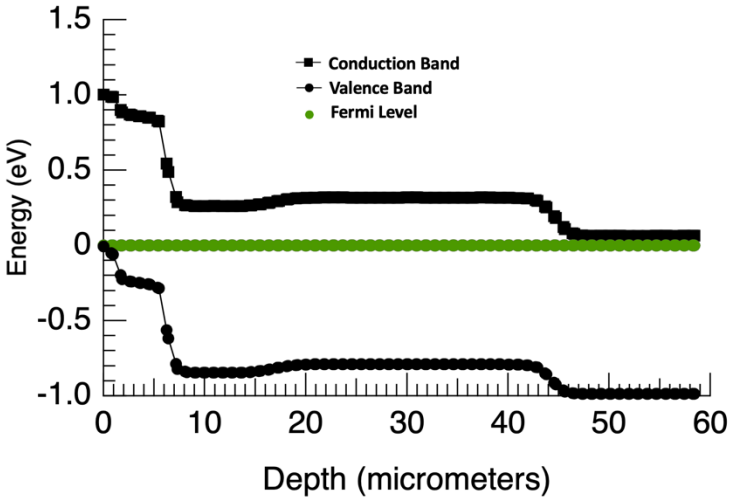

Figure II. 2. Bandgap diagram of the Si APD with no applied voltage.

SRH recombination and generation is a process that involves four processes: electron capture, electron emission, hole capture, and hole emission. It is represented as a function that considers electron minority carrier lifetime, τ_n (in a doped p-type material), hole minority carrier lifetime, τ_p (in a doped n-type material), intrinsic level, E_i, and recombination level, E_t.

$$R_{(SRH)} = \frac{np - {n^2}_i}{\tau_p(n + n_1) + \tau_n(p + p_1)} \qquad (II.1)$$

$$n_1 = n_i \exp\left(\frac{E_t - E_i}{n_i T}\right) \qquad (II.2)$$

$$p_1 = n_i \exp\left(\frac{E_i - E_t}{k_B T}\right) \quad (II.3)$$

Intrinsic level, E_i, and recombination level, E_t, are determined, in part, by the material's temperature and number of impurities/defects. For example, at room temperature (T) 300 K for silicon, E_i is 0.56 eV because it is near the middle of its bandgap of 1.12 eV, and $k_B T$ is 0.0259 eV. Meanwhile, carrier lifetimes, τ_n and τ_p, are defined as the average time before these minorities carriers recombine. For example, a silicon pn junction device at 300 K will have a τ_n at around 23.5 μs and a τ_p at around 1.5 μs [21]. Because silicon is an indirect bandgap material, these lifetimes are strongly dominated by SRH. This is because an indirect bandgap material largely emits photons when lattice defects are present within the material's bandgap [22], which is typically introduced with n-type doping and/or p-type doping.

SRH recombination takes advantage of these defects (also known as energy states) by moving electron and hole populations between the band edges (conduction band and valence band) through them. Specifically, an electron (or hole) becomes trapped by an energy state in this bandgap region. Then, depending on whether the hole (or electron) moves up to the same energy state before the electron (or hole) is thermally re-emitted into the conduction band, it may recombine. Meanwhile, the majority carriers are quickly captured in these localized states. As a result, SRH recombination and generation is determined by the number of impurities in the silicon because that influences the number of energy states.

Two other recombination mechanisms exist but are not considered relevant in this study's Si APD: radiative recombination and Auger recombination. Radiative recombination is predominantly a direct bandgap process that involves direct electron combination with a hole in the conduction band, and as mentioned, silicon is an indirect bandgap material. Meanwhile, Auger recombination occurs at high carrier densities, which is not a characteristic of this Si APD based on its doping profile (Figure I.1).

II.5 Avalanche Breakdown Definition

Avalanche gain occurs within the space-charge region of a reverse-biased pn junction when an electron attains enough energy from an electric field, $\mathcal{E}$, to break the bond between one of the atoms in the device lattice and one of the atom's electrons during a collision. This phenomenon is demonstrated in Figure II.3, which provides a general overview of the avalanche process [23]. As

mentioned, the process begins when an excited electron collides with the device lattice inside the space-charge region of a reverse-biased pn junction. It results in three carriers: the initial electron, the electron created from the collision, and the hole created from the collision. The incident electron is represented as a wavy arrow entering the pn junction. The straight arrows emitting from the 'x' are the three carriers. Due to drift caused by the electric field, the electrons move toward the n-type region and the hole moves toward the p-type region.

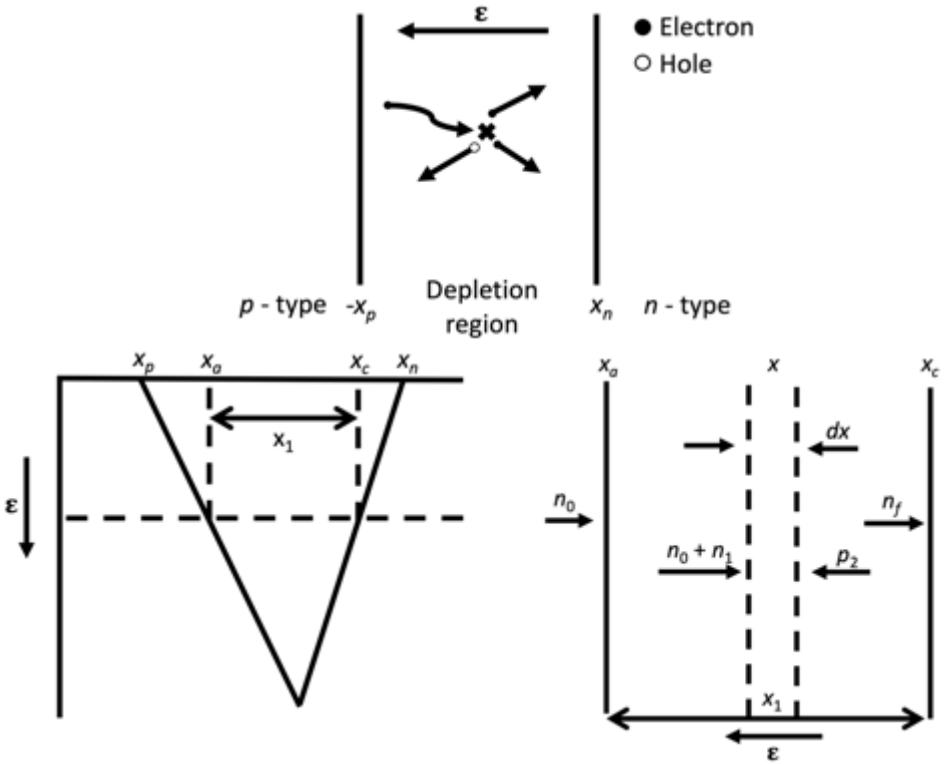

Figure II.3. Avalanche process (top). Schematic of carrier motion through space-charge region, and electric field position (bottom).

II.6 Generated Charge Definition

Experimentally, an APD's avalanche gain is related to the ratio of collected charge, Q_{coll}, to deposited charge, Q_{dep}. In other words, gain reflects how much charge is outputted from the APD relative to the amount of charge entering it. Deposited charge can be calculated by taking the integral of the linear energy transfer, LET(z), of the incident ion through the device lattice (Equation II.6). Figure II. 4 demonstrates the linear energy transfer, LET(z), of a 5.486 MeV alpha particle through silicon, which is the ion under consideration in this study [24]. LET(z) is the rate

of change of the electronic stopping energy $E_{elec}(z)$ of the ion as it moves through a material in units of $\frac{MeV*cm^2}{mg}$.

$$LET(z) = -\frac{1}{\rho}\frac{dE_{elec}(z)}{dz} \quad (II.4)$$

$$Q_{dep} = \frac{q\,\rho}{E_{ehp}}\int_0^{D_{ion}} LET(z)dz \quad (II.5)$$

The constants for the above equations are defined as follows: ρ is the density of silicon, E_{ehp} is the energy required to create an electron-hole pair in silicon (3.6 eV/ehp), and D_{ion} is the depth traveled by the ion. An important ratio for converting pC to MeV for silicon is 22.5 MeV/pC.

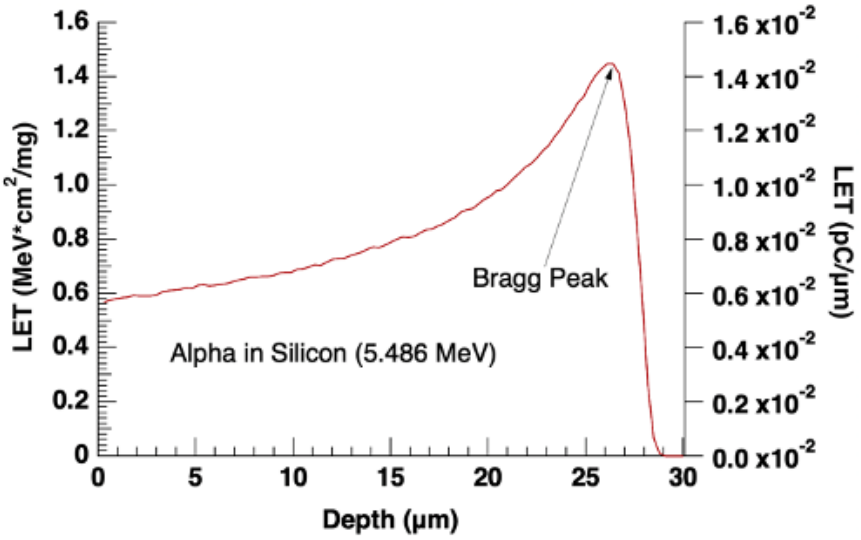

Figure II. 4. Linear energy transfer (LET) of a 5.486 MeV alpha particle through silicon.

II.7 Previous Research on APDs

Prior research has shown that an APD can measure generated charge by charged particle irradiation, as shown in Fig. 4.4.1 from [1]. Distribution of collected charge values resulting from incident gamma rays and alpha particles shows that collected charge produced by 5.11 MeV alpha particles weakly depends on reverse bias. Unfortunately, the literature is limited in explaining APD's charge collection mechanisms [1]. Two Si APDs and one InGaAs APD were tested, and they found that these ionizing particles resulted in pulses of a smaller gain compared to pulses from energetic photons with respect to increasing reverse bias. A notable difference between the tested devices was that the APD used in this work had a capacitance of 270 pF and a surface area

of 100 mm^2 [20], while the capacitances and surface areas of the APDs in [1] were all around 2 pF and 1 mm^2, respectively. A larger capacitance requires more deposited charge to output the same signal from the APD as compared to one with a smaller capacitance. The APD's large capacitance did not have a noticeable effect on the observed results compared to the charge distribution plot (Fig. 4.4.1 from [1].).

The S8664-1010 APD was most recently used in CERN's Large Hadron Collider to detect low light yields from colliding particles [25]. The CERN team chose an APD with a surface area relatively larger than the typical photodiode to maximize the number of photons colliding with the detector per mm^2. In our case, the S8664-1010 APD was used to maximize the number of alpha particles produced by an Am^{241} button source colliding with the detector. Other studies have also attempted to explain the effects of radiation particles on Si APDs [26] [27]. The experiments discussed in [26] and [27] focused on the feasibility of small satellites using APDs in LEO to detect ionizing and non-ionizing particles.

CHAPTER III

EXPERIMENTAL SETUP AND PROCEDURES

III.1 Test Structures

A short-wavelength Si APD (S8664-1010) was acquired from Hamamatsu Photonics. A cross section of this type of diode is shown in Figure III.1 [28]. When exposed to photons, the APD multiplies the charge through avalanching when charge carriers are accelerated by the device's electric field after exceeding a diode-specific voltage in reverse bias (>200 V in our case) [20]. At these reverse biases, a photon first passes the epoxy layer labeled 'AR (anti-reflection) coating.' The epoxy improves the quantum efficiency of the device by reducing reflection loss. The photon then enters through the contact layer. The anode is located here and is held at ground. Light is then absorbed in the collection region, where it undergoes the photoelectric effect [28]. E-h pairs are generated. This is a significant feature of the photodiode because it allows these pairs to be generated before reaching the depletion region. The depletion region is where the electric field peaks (Figure III.1), which allows for electron drift that leads to the avalanche effect producing gain. The gain in the output signal allows low photon counts to be detectable. The gain response from the APD's documentation can be found in Figure III.2 [20]. The simulated gain response for the APD (Figure III.2) will be discussed later.

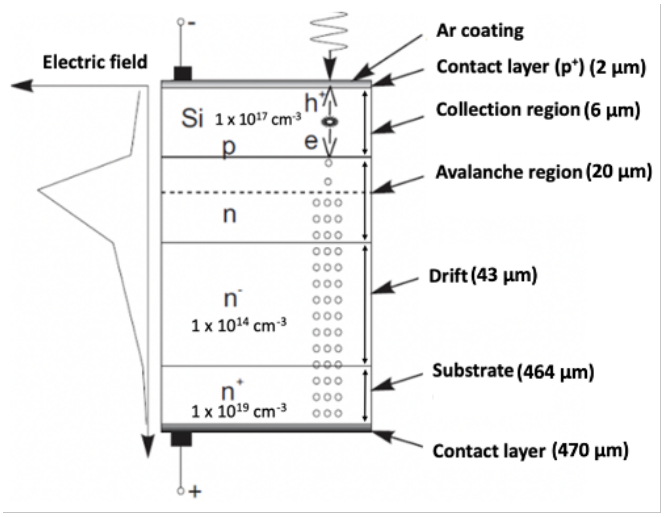

Figure III.1. A concept of an Si APD for short-wavelength light detection. Based on [28]. Not drawn to scale.

The CubeSat application mentioned in the introduction uses an APD combined with a scintillator crystal to enhance signals produced from photon absorption. The scintillator crystal used is $^{6}LiInSe_2$ and covers the Si APD's entire surface area. Furthermore, it converts the thermal neutrons into photons. 21,000 photons [3] with wavelengths ranging from 400 to 800 nm, and peaked at ~510 nm (see Fig. 4 in [20]), are produced per thermal neutron collision. (This APD design enables photon detection for wavelengths between 320 nm and 1000 nm [20]. This wavelength range is a key reason the APD was chosen for the crystal.) And finally, generated charge through photon absorption is spatially uncorrelated within the APD, unlike for an ion.

A ~5.5 MeV alpha particle is also produced via thermal neutron capture as a reaction product. This alpha particle can get passed through the APD if formed between the APD and the scintillator. Furthermore, the space environment contains many alpha particles. As a result, this study focuses on the responses from both 420 nm photons and ~5.5 MeV alphas.

It is also important to note that gain is not exclusive to electrons. Holes can also experience gain, which leads to signal masking in the form of dark current. For our Si APD, holes that enter the avalanche region from the drift region undergo a smaller gain relative to the electrons [28]. This is because the multiplication factor for holes is smaller than that for electrons [29]. The electrons then enter the substrate, which is the region of our APD that leads to the back contact. Then, electrons are collected via drift from the back contact. The cathode is located here as well, where positive bias is applied. This is so that the diode can be fully depleted and allow for drift under reverse bias. The total collected charge is significantly higher than the charge generated by the photon spectrum because of avalanche.

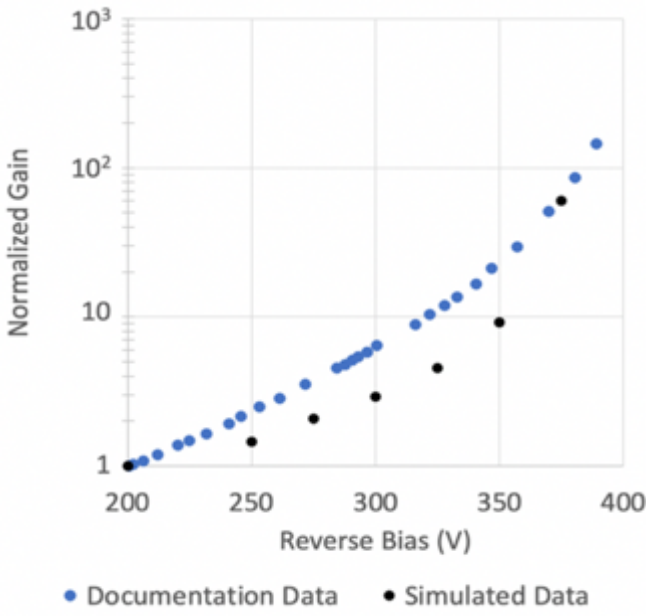

Figure III.2. Documentation gain vs. simulated gain of a continuous wave of 420 nm photons from the Si APD.

III.2 Experimental Setup

The APD was delivered with an epoxy layer on top of the APD (Figure III.*3*), which was removed prior to any experimental testing to reduce attenuation of the alpha particle energy. Alpha irradiation was performed at Vanderbilt using a 10 μCi button source of Americium-241 with a surface area of 100 mm^2. The Si APD and button source were placed 152.4 mm apart from each other to detect particle strikes as close to normal incidence as possible. This distance was calculated to ensure 1 particle strike per second per mm^2 (100 particle strikes per second for the entire diode) at angles up to 13˚. The APD was shielded from ambient light and RF noise, and then placed in the vacuum chamber in total darkness at room temperature (25˚C). Alpha irradiations at reverse biases of 0 V, 50 V, 100 V, 150 V, 200 V, 250 V, 300 V, 350 V, and 400 V each lasting 1000 seconds were conducted.

A pulse-height analysis (PHA) setup was used to measure the charge collection spectrum [30]. The setup converted each current transient into a voltage pulse, recorded the pulse's height, and saved the total number of pulses of each height per channel. (Current transients from the APD were fed into a Ortec 142A preamplifier, which then went into an Ortec amplifier. The amplifier pulses went into an Ortec MCA (multichannel analyzer), which was then read via computer through Ortec's MAESTRO MCA emulation software.) Each channel in this histogram was then matched to an energy range by calibrating the diode to a radiation source where the channel-to-energy ratio was already known for a different diode. In this case, it was a surface barrier detector (SBD) with a known PHA calibration using Am^{241} [31]. Low-channel noise was removed from all runs by setting a noise discriminator to channel 100 (equivalent to ~1 MeV). A pulser was used to aid in the APD's calibration by aligning the pulses found in the SBD to the APD.

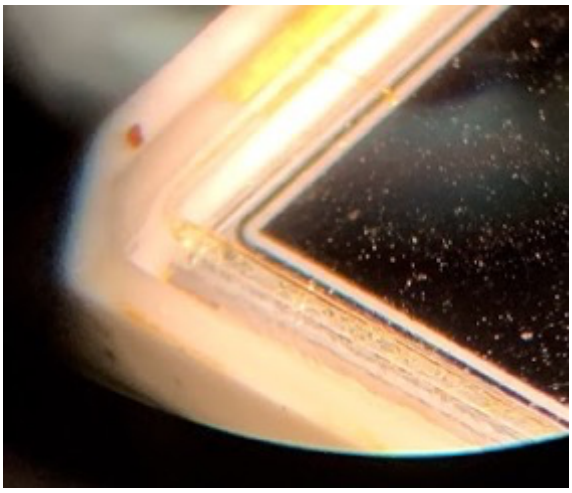

Figure III.3. Close-up of epoxy on the APD (Credits: Professor Enxia Zhang)

III.3 Calculating Voltage Output

When measuring the voltage output of the Ortec 142A preamplifier, we found that the multimeter was reading an output 10% less than the incoming voltage from the power supply. It was determined that this discrepancy had to do with the input impedance of the multimeter itself. Finding the total resistance and total current of the setup resulted in the correct valuation of the voltage output. A schematic of this setup can be found in Figure III.4.

To find the total resistance, the resistors in the preamplifier (101.5 MΩ in total) is in series with the input resistor of the multimeter (10 MΩ for a Fluke 115 multimeter). However, the multimeter's resistor is in parallel with the power supply's resistor (1 MΩ). As a result, the calculated resistor value in parallel between the two devices is 909.1 kΩ. Leading to the total resistance of the circuit being 102.4 MΩ.

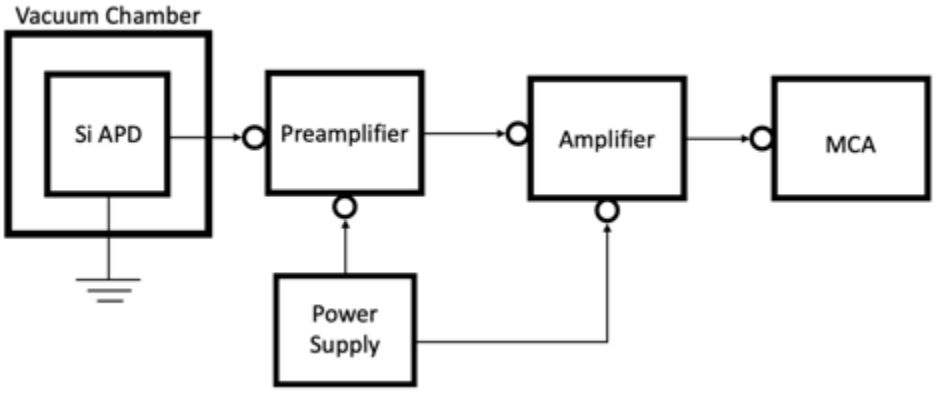

Figure III.4. Schematic of PHA Setup

Then, to find the current, Equation III.1 was used from the power supply's documentation to get a value of 1.012 μA [32].

$$I_D = \frac{V_M(R_P + 1 * 10^6)}{R_P(1 * 10^6)} \quad (III.1)$$

I_D refers to detector current, V_M refers to measured voltage, and R_P refers to the input resistance of the multimeter.

Equation III.2 was then used to find the output voltage to be 103.6 V, which is approximately equal to the 100 volts.

$$V = I * R \quad (III.2)$$

III.4 Energy Resolution

Energy resolution is another important parameter to consider because it allows us to understand how well the device can differentiate between these particles. The lower the energy resolution is equivalent to better detection, as shown in Equation III.3.

$$Energy\ Resolution\ (\%) = \frac{FWHM}{Channel\ Peak} \quad (III.3)$$

The energy resolution was calculated in a vacuum chamber at Vanderbilt University (Table III.1). Without the epoxy layer and in a vacuum, the APD was more sensitive toward the alpha

energies at operating reverse bias and above for the reasons mentioned above, resulting in narrower pulses. For background, alpha decay from ^{241}Am results in 5.443 MeV particles (13.0% of the time), 5.486 MeV particles (85% of the time), and 5.388 MeV particles (2% of the time). They also decay into 59 keV gamma rays.

Table III.1. Energy Resolutions of Alphas Produced by Americium-241

Button Source	Reverse Bias (V)	FWHM	Channel Peak	Energy Resolution (%)
Americium-241	0	79	687	11.50
Americium-241	50	100	3070	3.26
Americium-241	100	300	4100	7.32
Americium-241	150	600	4850	12.37
Americium-241	200	907	5300	17.11
Americium-241	250	1000	5480	18.25
Americium-241	300	1020	5660	18.02
Americium-241	350	1653	5500	30.05
Americium-241	400	2300	6000	38.33
Americium-241	450	2300	5800	39.66

III.5 Data Analysis

A thorough understanding of the charge collection processes within the Si APD can provide insight into its avalanche effect. By considering the depletion approximation, we can use Poisson's equation to determine the maximum electric field observed in the Si APD and compare it against the breakdown electric field necessary to induce avalanche. Using this approximation allows us to view the space-charge as a region confined to a distance of x_d units. It also allows us to assume the electric field's magnitude decreases linearly as a function of position. Meanwhile, Poisson's equation provides insight into the relationship of a pn junction's carrier concentrations to its dopants by relating the device's charge density ρ (charge/cm^3) to the potential gradient of its electric field $\boldsymbol{\nabla} * \boldsymbol{\mathcal{E}}$:

$$\boldsymbol{\nabla} * \boldsymbol{\mathcal{E}} = \rho / K_S \varepsilon_0 \qquad (III.4)$$

K_S is the semiconductor dielectric constant and ε_0 is the permittivity of free space. The charge density ρ can be found using the following equation:

$$\rho = \frac{q}{\epsilon_s}(p - n + {N_D}^+ - {N_A}^-) \qquad (III.5)$$

where p is the total number of holes per cm^3 in the valence band, q is the electronic charge, ϵ_s is the relative permittivity of the material, n is the total number of electrons per cm^3 in the conduction band, ${N_D}^+$ is the number of ionized donors per cm^3, and ${N_A}^-$ is the number of ionized acceptors per cm^3.

A combination of these equations and this assumption allows us to divide the pn junction into distinct zones that are either 'neutral' or 'completely depleted of mobile carriers.' In this depletion region (the area between $-x_p$ and x_n, shown in Equations III.6 and III.7), we expect the charge density to equal the ionized dopant concentration. Integrating Poisson's equation given this assumption produces the following equations for electric field, which varies depending on the region in which they are found:

$$\varepsilon(x) = -\frac{qN_d}{\epsilon_s}(x_n - x);\ for\ 0 < x < x_n, \qquad (n - region) \qquad (III.6)$$

$$\varepsilon(x) = -\frac{qN_a}{\epsilon_s}(x + x_p);\ for\ -x_p < x < 0, \qquad (p - region) \qquad (III.7)$$

This integration tells us that we should expect the peak electric field to occur where these two regions meet. It also tells us that the depletion region's width varies inversely with the magnitude of the dopant concentration and can be represented by Equation III.8:

$$N_a x_p = N_d x_n \qquad (III.8)$$

In other words, increasing dopant concentration corresponds to a smaller space-charge region. In our case, the APD is highly asymmetrical in which the lighter doped region is the n-region at around $n = 3.16 * 10^{14}\ \mathrm{cm}^{-3}$. Meanwhile, the heavier doped p-region is around $3.16 * 10^{16}\ \mathrm{cm}^{-3}$. Therefore, the depletion region moves into the lightly doped n-region of $3.16 * 10^{14}\ \mathrm{cm}^{-3}$, which extends to 40 μm before reaching a heavily doped n-region of $3.16 * 10^{16}\ \mathrm{cm}^{-3}$.

Using these values, we can then calculate the expected maximum electric field at each reverse bias from 0 V to 450 V in increments of 50 V. The maximum electric field at each reverse bias provides a measure of determining when the breakdown electric field is exceeded, and thus inducing impact ionization. We use Equation III.9 to calculate the maximum electric field at each reverse bias increment, which is plotted in Figure III.5.

$$\varepsilon_{max} = \left(\frac{2qN_d|V_R|}{\epsilon_s}\right)^{\frac{1}{2}} \ where\ N_d \ll N_a \qquad (III.9)$$

Given these values, we now need to determine the breakdown electric field. Hamamatsu provides us with that number, which is 200 V, but it is possible to independently derive it as well. First, we find the value for the breakdown electric field in silicon. Given that this field is dependent on the lighter doped region in a doping profile, we can determine that this field is around $1.51 * 10^5\ \mathrm{V\ cm}^{-1}$ for an N concentration of $3.98 * 10^{14}\ \mathrm{cm}^{-3}$.

$$BV = \frac{\epsilon_s \varepsilon^2{}_1}{2qN_a} \qquad (III.10)$$

Plugging these values into Equation III. 10 for breakdown voltage gives 186 V. This value is very close to the Hamamatsu's measurements for the start of gain.

$$\frac{11.68 * (8.865 * 10^{-14}\ \mathrm{F\ cm}^{-1}) * (1.51 * 10^5\ \mathrm{V\ cm}^{-1})^2}{2 * (1.6 * 10^{-19}\ \mathrm{C}) * 3.98 * 10^{14}\ \mathrm{cm}^{-3}} = 186\ \mathrm{V}$$

Given this rationale, our expectation is that charged carriers generated by alpha particles should undergo gain beginning at a reverse bias of 186 V. The breakdown electric field presents a breakdown reverse bias slightly higher than 200 V (based on eyeballing Figure 4.14 from [23]).

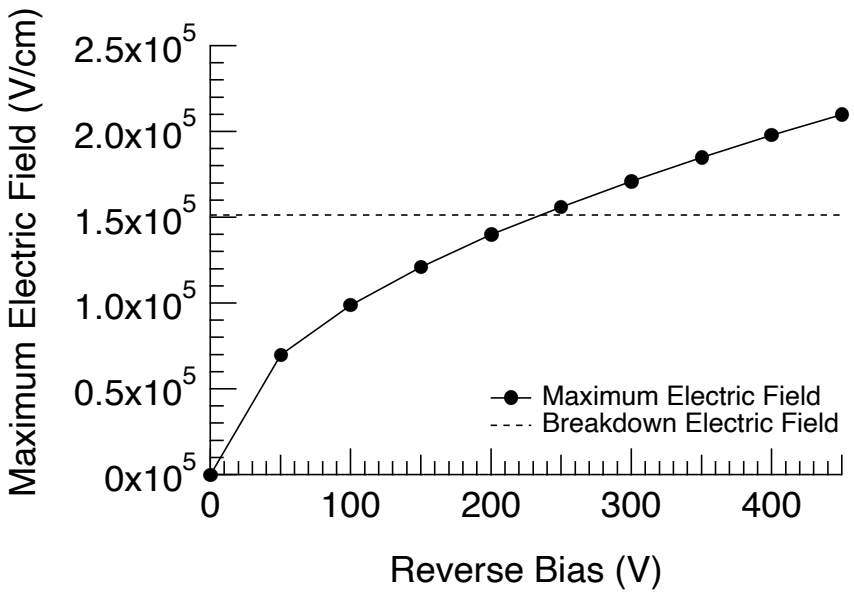

Figure III.5. Maximum electric field (V cm^{-1}) vs. reverse bias (V) with breakdown electric field

CHAPTER IV

DISCUSSION

Figure IV. 1 shows the pulse height spectrum created during the ten runs, color-coded according to the applied reverse bias, and plotted by energy (MeV) vs. total number of counts. When the applied reverse bias increases from 0 V to 200 V, the peak shifts to higher energy levels. This is attributed to the increased depletion region with bias, resulting in more charge being collected. For reverse biases larger than 200 V, the peak saturates near 5 MeV, just short of the full 5.5 MeV alpha particle energy. The slight difference is due to a small amount of energy loss in the overlayer materials. Next, we use TCAD to investigate the results for reverse bias > 200 V.

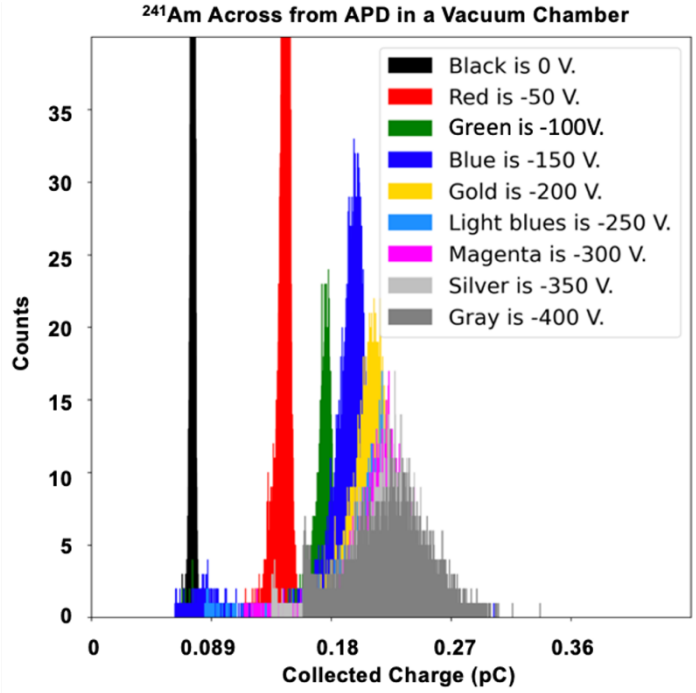

Figure IV. 1: Pulse charge distribution plot of ~5.5 MeV alpha particles from a 10 µCi Am241 button source through the experiment's 100 mm2 Si APD placed in a stainless-steel vacuum chamber.

The doping profile used in TCAD is the one seen in Figure I.1. The measurements are recalculated to provide doping profiles, which are then read into Sentaurus TCAD via a text file. Sentaurus TCAD allows devices to be tested for various radiation environment based on their doping profiles. Even though the doping profile extends to 470 µm, a doping profile limited to 60 micrometers is incorporated because the doping was found to remain at n^+ after that depth.

Once the file is read into Sentaurus TCAD, the Si APD's width is set to a cylindrical area equal to the true diode's area for 2D cylindrical transient simulations. To confirm the doping profile is correctly inputted into TCAD, the experimentally derived doping profile is simulated. The two doping profiles were found to match (Figure I.1 to Figure IV.2).

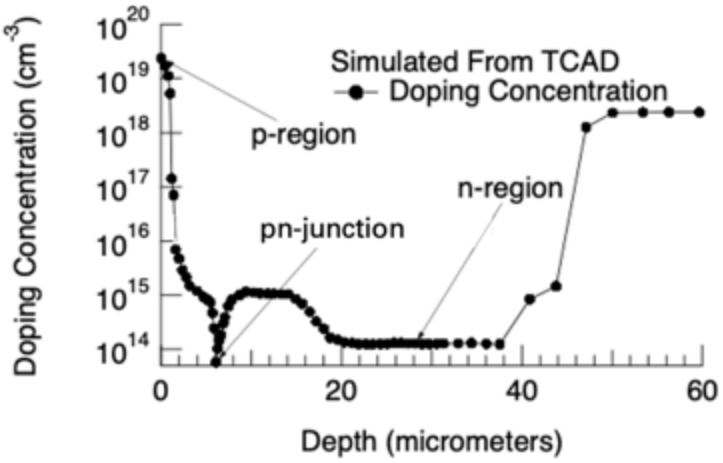

Figure IV.2. Doping profile (combined electrons and holes) of the Si APD as outputted by TCAD.

Another simulated plot is the electric field under reverse bias at 400 V, which is used to check against the known electric field shape of the Si APD (Figure IV.3), as well as the known maximum value of the electric field (2.5 * 10^5 V/cm) [28]. The plots and maximum values matched each other.

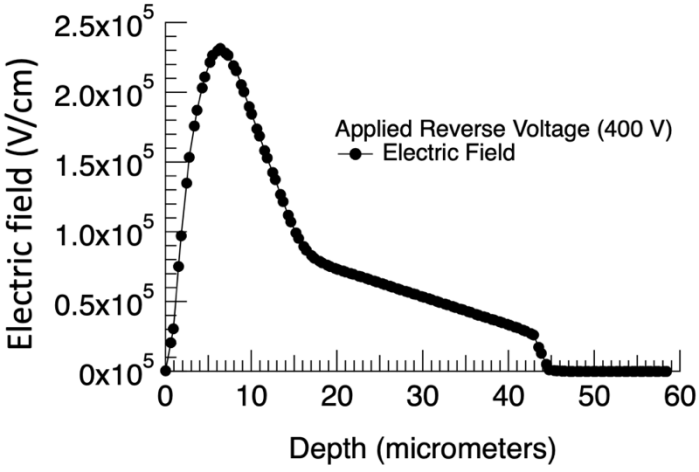

Figure IV.3. Electric field of the APD under reverse bias of 400V.

The avalanche generation model used is the van Overstraeten-de Man model [33]. This model is distinct from alternative TCAD avalanche models because it is based on empirical data that

prioritized electric fields between 1.75 x 10^5 $\frac{\mathrm{V}}{\mathrm{cm}}$ to 6 x 10^5 $\frac{\mathrm{V}}{\mathrm{cm}}$. This worked well with the APD, because based on its doping profile, the APD has a breakdown electric field of ~3 x 10^5 $\frac{\mathrm{V}}{\mathrm{cm}}$. The model's equation can be found below [34]:

$$\alpha_{n(p)} = a_{n(p)} e^{-\frac{b_{n(p)}}{\varepsilon}} \qquad (IV.1)$$

The variables are defined as the following: $\vec{\mathcal{E}}$ is the electric field within the APD at a given reverse bias. $\mathrm{A_{n(p)}}$ $\left(\frac{1}{\mathrm{cm}}\right)$ is the ionization coefficient [34], $\mathrm{a_{n(p)}}$ $\left(\frac{1}{\mathrm{cm}}\right)$ is the maximum number of carriers that can be generated per unit distance at very high electric fields, and $\mathrm{b_{n(p)}}$ $\left(\frac{\mathrm{V}}{\mathrm{cm}}\right)$ is the critical field constant for electrons or holes, depending on what is being calculated. It is related to the ionization energy and the mean free path of the carriers between ionizing collisions [35].

An electrical breakdown simulation is also run to calibrate the TCAD model (Figure IV. 4), and it is found that the APD's simulated breakdown closely matches that from the APD data sheet [20]. The data sheet also shows how the enhanced charge of the APD as a function of reverse bias changes in response to a 420 nm continuous optical wave. Optical simulations with an intensity of 0.1 W/s and a wavelength of 420 nm were also run for calibration purposes (Figure III.2). It was found that the simulated electrical breakdown and optical gain agree with the data sheet.

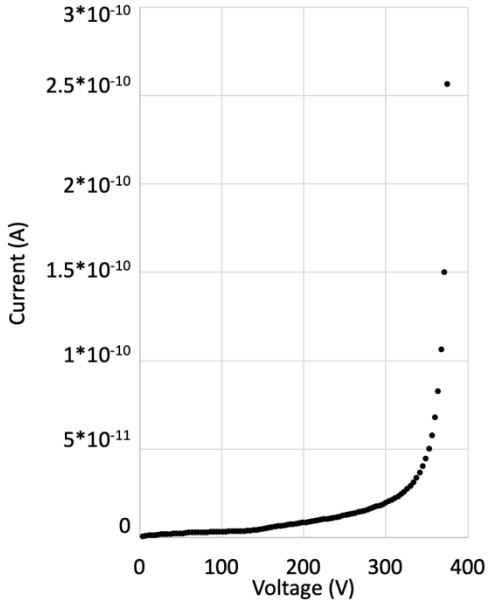

Figure IV. 4. I-V curve showing electric breakdown.

The calibrated TCAD model created simulations of 5.5 MeV alpha particles where the total collected charge is ~0.27 pC at a reverse bias of 200 V. The collected charge is ~0.65 pC at a reverse bias of 400 V. It is found that a small amount of charge enhancement ($charge_{400V}/charge_{200V}$ = 2.5x) occurs but is lower than the static DC normalized gain at 400 V associated with a photon CW (>100x) (Figure III.*2*). Meanwhile, TCAD simulated photon irradiation agrees with the $charge_{400V}/charge_{200V}$ = 100x. This is because a transient ion is different from a continuous wave of photons. As the ion vertically moves through the device, it creates a spatially localized and highly localized track of charge. A large portion of the depletion region is also passed, resulting in carriers being collected, avalanching, or recombining. The charge transport mechanisms in this region are affected by this highly localized plasma. This is not the case for photons generated spatially uncorrelated charge. To highlight this point, TCAD results show that generated charge from avalanche is larger for photon irradiation compared to ion irradiation.

Transient optical simulations are run to compare alpha response to spatially uncorrelated photon response. Figure IV.5 shows the current transients from these simulations, where the simulated photon waves have durations of either 10 ns or 100 ps. The current reaches steady state for the 10 ns photon wave and can be considered continuous and analogous to the static DC continuous wave condition. The 10 ns and 100 ps photon waves at bias conditions 200 V and 400 V have two orders of magnitude separating the peak currents. This matches the APD data sheet, which shows a normalized gain of ~100x at these bias conditions (Figure III.3). Furthermore, the photon's rise time is different from that of the alphas. This is because the CW is laterally spread throughout the device with a lower peak charge density. However, a much wider region of impact causes more total charge. Significant avalanche occurs for a long period when this charge is deposited mostly within the device's avalanching region. This contrasts with the alpha particle strike's behavior.

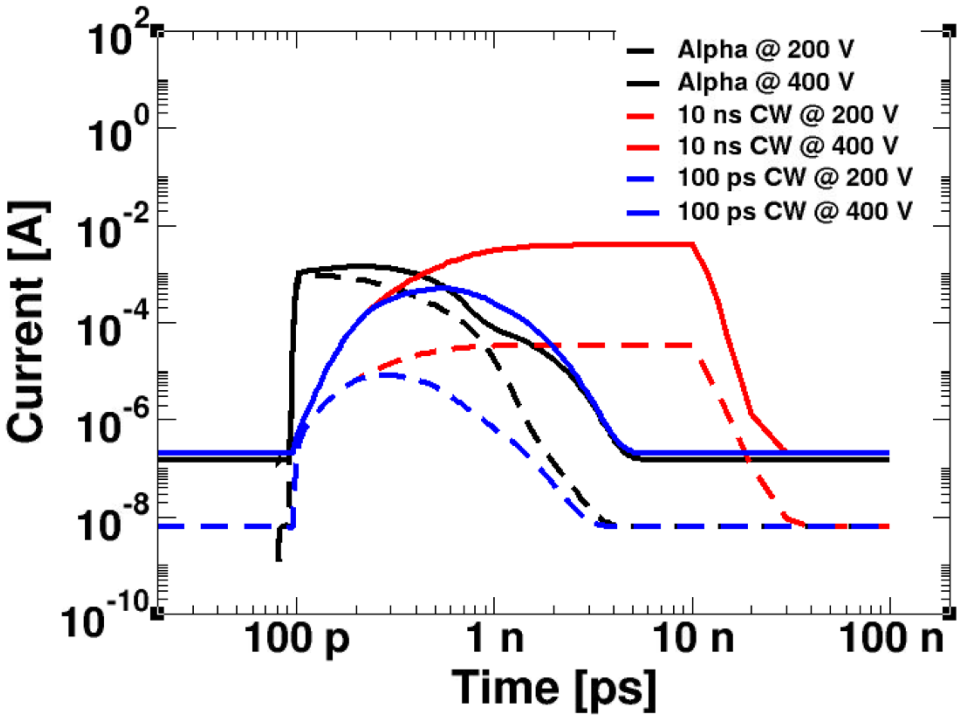

Figure IV.5. Time Signature comparison for alphas and 510 nm photons.

CHAPTER V

CONCLUSIONS

APDs tend to be used to detect low levels of photons because its intrinsic charge enhancement allows photons to be observed above the background noise. Alternative detectors (e.g., surface barrier detectors) do not have such intrinsic charge enhancement.

This work examines the generated charge characteristics of a Si APD in response to Am^{241} alpha particles. Trends are found experimentally using a pulse height analysis setup that measure the number of counts detected at reverse bias from 0 V to 400 V in increments of 50 V with respect to collected charge. An LET curve is used to determine the amount of deposited charge from the alpha particle used (~5.5 MeV alpha). Furthermore, as discussed in the introduction, a CubeSat mission is being created to observe thermal neutrons using an APD. 420 nm photons and 5.5 MeV alphas were considered.

Figure IV.5 shows a calibrated TCAD simulation of current transients that show a great difference between alpha particles and photons. While the alphas reveal a fast rise time, the photons do not. Peak current is also not bias-dependent for alphas. A peak current gain of approximately 1x is found. Meanwhile, photon waves show a peak current that is strongly bias-dependent. They have peak current gain of approximately 100x. And finally, the photon's rising edge profile is significantly reduced when compared to that from alphas.

REFERENCES

[1] H. N. Becker and J. S. Laird, “Transient Effects in Silicon and InGaAs Avalanche Photodiodes,” *NEPP FY05 Sens. Technol. Radiat. Task*, p. 12, Oct. 2005.

[2] J. C. Egner *et al.*, “Integration of a $^{6}LiInSe_2$ Thermal Neutron Detector into a CubeSat Instrument,” *J. Astron. Telesc. Instrum. Syst.*, vol. 2, no. 4, p. 6, Oct. 2016.

[3] M. M. Nieto, W. C. Feldman, and D. J. Lawrence, “Testing The Unitarity Of The Ckm Matrix With A Space-Based Neutron Decay Experiment,” *Mod. Phys. Lett. A*, vol. 23, no. 21, pp. 1735–1743, Oct. 2008, doi: 10.1142/s0217732308027187.

[4] A. Waczynski *et al.*, “HgCdTe Detectors for the Hubble Space Telescope Wide Field Camera 3 IR Channel,” in *Scientific Detectors for Astronomy*, Dordrecht, 2004, pp. 175–182. doi: 10.1007/1-4020-2527-0_20.

[5] C. W. Stubbs *et al.*, “PRECISE THROUGHPUT DETERMINATION OF THE PanSTARRS TELESCOPE AND THE GIGAPIXEL IMAGER USING A CALIBRATED SILICON PHOTODIODE AND A TUNABLE LASER: INITIAL RESULTS,” *Astrophys. J. Suppl. Ser.*, vol. 191, no. 2, pp. 376–388, Dec. 2010, doi: 10.1088/0067-0049/191/2/376.

[6] X. Sun *et al.*, “Proton Radiation Effects on HgCdTe Avalanche Photodiode Detectors,” *IEEE Trans. Nucl. Sci.*, vol. 68, no. 1, pp. 27–35, Jan. 2021, doi: 10.1109/TNS.2020.3040741.

[7] “photoelectric effect | Definition, Examples, & Applications,” *Encyclopedia Britannica*. https://www.britannica.com/science/photoelectric-effect (accessed Mar. 06, 2021).

[8] E. M. D. Fisher, “Principles and Early Historical Development of Silicon Avalanche and Geiger-Mode Photodiodes,” *Photon Count. - Fundam. Appl.*, Dec. 2017, doi: 10.5772/intechopen.72148.

[9] “History of Vacuum Tube / Thermionic Valve » Electronics Notes,” *electronics notes*. https://www.electronics-notes.com/articles/history/vacuum-tube-thermionic-valve/history.php (accessed Apr. 21, 2021).

[10] V. K. Zworykin, G. A. Morton, and L. Malter, “The Secondary Emission Multiplier-A New Electronic Device,” *Proc. Inst. Radio Eng.*, vol. 24, no. 3, pp. 351–375, Mar. 1936, doi: 10.1109/JRPROC.1936.226435.

[11] “Photomultiplier Handbook,” Burle Technologies, Inc., USA, 1980. Accessed: Mar. 06, 2021. [Online]. Available: https://psec.uchicago.edu/links/Photomultiplier_Handbook.pdf

[12] “Photomultiplier Tubes,” Hamamatsu Photonics K. K., 2007. Accessed: Mar. 06, 2021. [Online]. Available: https://www.hamamatsu.com/resources/pdf/etd/PMT_handbook_v3aE.pdf

[13] E. Hergert and Hamamatsu Corporation, “Detectors: Guideposts on the Road to Selection,” *Photonics marketplace*. https://www.photonics.com/Articles/Detectors_Guideposts_on_the_Road_to_Selection/a25535 (accessed Mar. 06, 2021).

[14] mks | Newport, “Photomultiplier Tubes,” *Newport*, 2021. https://www.newport.com/f/photomultiplier-tubes (accessed Mar. 07, 2021).

[15] Digi-Key, “Sensors, Transducers | Optical Sensors - Photodiodes | DigiKey,” *Digi-Key*, 2021. https://www.digikey.com/en/products/filter/optical-sensors-photodiodes/543?s=N4IgTCBcDaIIYDc4Bs4DsDGALApgAgAcsB7AF2IBMBLSnEAXQF8g (accessed Mar. 07, 2021).

[16] J. Nishizawa, “P-I-N Photo-Diode,” #JP1955-8969A

[17] W. Shockley, M. Sparks, and G. K. Teal, “p-n Junction Transistors,” *Phys. Rev.*, vol. 83, no. 1, pp. 151–162, Jul. 1951, doi: 10.1103/PhysRev.83.151.
[18] K. G. McKay and K. B. McAfee, “Electron Multiplication in Silicon and Germanium,” *Phys. Rev.*, vol. 91, no. 5, pp. 1079–1084, Sep. 1953, doi: 10.1103/PhysRev.91.1079.
[19] Ashish, “What is the Photoelectric Effect? » Science ABC,” *Science ABC*, 20 2017. https://www.scienceabc.com/pure-sciences/what-explain-photoelectric-effect-einstein-definition-exmaple-applications-threshold-frequency.html
[20] Hamamatsu, “Si APD - Hamamatsu Photonics: S8664 Series,” *Hamamatsu*. https://www.hamamatsu.com/resources/pdf/ssd/s8664_series_kapd1012e.pdf
[21] W. Zimmerman, “Experimental verification of the Shockley–Read–Hall recombination theory in silicon,” *Electron. Lett.*, vol. 9, no. 16, pp. 378–379, Aug. 1973, doi: 10.1049/el:19730279.
[22] H. Föll, “2.3.3 Shockley-Read-Hall Recombination,” *Semiconductors I*, Oct. 2019. https://www.tf.uni-kiel.de/matwis/amat/semi_en/kap_2/backbone/r2_3_3.html (accessed Apr. 22, 2021).
[23] R. S. Muller, T. I. Kamins, and M. Chan, *Device Electronics for Integrated Circuits*, 3rd edition. New York, NY: Wiley, 2002.
[24] J. F. Ziegler, “SRIM - The Stopping and Range of Ions in Matter,” Jul. 2019. http://www.srim.org/
[25] W. Erni, Y. Heng, and F. H. Heinsius, “Technical Design Report for: PANDA Electromagnetic Calorimeter (EMC),” PANDA, 2008.
[26] J. Kataoka *et al.*, “In-orbit performance of avalanche photodiode as radiation detector on board the picosatellite Cute-1.7 APD II,” *J. Geophys. Res. Space Phys.*, vol. 115, no. A05204, pp. 1–9, 2010, doi: 10.1029/2009ja014699.
[27] M. A. Nunes *et al.*, “Neutron-1 Mission: Low Earth Orbit Neutron Flux Detection and COSMOS Mission Operations Technology Demonstration,” 2019, pp. 1–15.
[28] D. Melnychuk and B. Zwieglinski, “Low-Energy Photon Detection with PWO-II Scintillators and Avalanche Photodiodes in Application to High-Energy Gamma-Ray Calorimetry,” *Intech Open Access Publ.*, pp. 1–16, 2011.
[29] Q. R. Baron, S. Kishimoto, J. Morse, and J.-M. Rigal, “Silicon avalanche photodiodes for direct detection of X-rays,” *J. Synchrotron Radiat.*, 2005.
[30] R. A. Reed, P. J. McNulty, W. J. Beauvais, and D. R. Roth, “Charge collection spectroscopy,” *IEEE Trans. Nucl. Sci.*, vol. 40, no. 6, pp. 1880–1887, Dec. 1993, doi: 10.1109/23.273466.
[31] “ULTRA and ULTRA AS: Ion-Implanted-Silicon Charged-Particle Detectors,” Ortec. Accessed: Jan. 26, 2021. [Online]. Available: https://www.ortec-online.com/-/media/ametekortec/brochures/ultra.pdf?dmc=1&la=en&revision=01d7fc9b-f814-489b-893b-5c3fd28d940a
[32] “Model 428 Detector Bias Supply Operating and Service Manual,” Advanced Measurement Technology, Inc., USA, 2020. [Online]. Available: https://www.ortec-online.com/-/media/ametekortec/manuals/428-mnl.pdf?dmc=1&la=en&revision=7f9e003b-cd05-48c6-aa7a-690d6c9db6b5
[33] “Synopsys TCAD Tools,” Synopsys, Inc., Mountain View, CA, 2013. [Online]. Available: http://www.synopsys.com
[34] Synopsys, *Sentaurus Device User Guide*. 2012.

[35] S. M. Y. Hasan, “Neutron irradiation effects on the breakdown voltage of power MOSFETs,” 1993, Accessed: Jan. 27, 2021. [Online]. Available: https://repository.arizona.edu/handle/10150/278361